ACS APPLIED ELECTRONIC MATERIALS

Article

pubs.acs.org/acsaelm

Controlling Magnetization of Gr/Ni Composite for Application in High-Performance Magnetic Sensors

Mohammadreza Hajiali,*[,†] Loghman Jamilpanah,[†] Zahra Sheykhifard,[†] Mahsa Mokhtarzadeh,[†] Hossein Yazdi,[†] Behnam Tork,[†] Javad Shoa e Gharehbagh,[†] Behnam Azizi,[†] Ehsan Roozmeh,[‡] Gholam Reza Jafari,[†] and Seyed Majid Mohseni*[,†]

[†]Faculty of Physics, Shahid Beheshti University, Evin, 19839 Tehran, Iran

[‡]Department of Physics, University of Kashan, 87317 Kashan, Iran

ABSTRACT: Graphene (Gr), a well-known 2D material, has been under intensive investigation in the past decade due to its high potential applications in industry and advanced technological elements. Composites made of Gr and other functional materials especially magnetic materials have opened opportunities in sensors, health care monitoring, magnetic devices, etc. Here, we report a mass production of Gr/Ni composite powders using an electrochemical exfoliation/deposition method with different magnetic strengths of the final composite material. We applied the magnetic composite materials in a magnetoimpedance (MI)-based sensor and observed a significant enhancement in the MI effect and its field sensitivity. Such magnetic composites with controlled magnetization strengths are coated on the MI-ribbon sensor surface, and different MI responses are observed. Furthermore, the MI response of a ribbon coated with a Gr/Ni layer is theoretically determined based on an electrodynamic model with a qualitative consistency to experimental results. Our comprehensive study can be applied in high-performance functionalized MI-based magnetic sensors and devices.

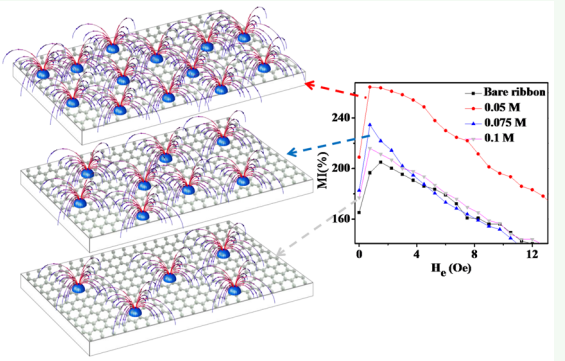

KEYWORDS: *surface modification, electrochemical exfoliation, magnetoimpedance sensor, graphene/nickle composite, magnetic nanoparticles*

1. INTRODUCTION

In recent years, graphene (Gr), a two-dimensional (2D) hexagonal lattice of sp^2 hybridized carbon atoms, has attracted comprehensive research interest because of its fascinating electrical, mechanical, chemical, and optical properties and its potential application in next-generation electronics,[1,2] energy storage devices,[3−5] and composite-based materials.[6−8] Integration of Gr or the Gr family with various nanoparticles (NPs) allows the development of new nanocomposite materials with novel properties and highly promising applications in bioscience,[9−11] microwave elements,[12,13] sensors,[14] etc.[15]

The formation of hybrid structures made of Gr and nanoparticles represents new functionality and properties which offer them for applications in technology and industry due to their developed characteristics related to separate counterparts.[16] Due to preserving the characteristics related to the NPs, Gr−nanoparticle hybrid structures are promising for their electronic, optical, structural, and magnetic properties that are unavailable in bulk materials. In addition to the above-mentioned properties they show the potential for use in bioapplications.[17] Specially, Gr materials are alluring when combined with magnetic NPs, for sensor and catalytic properties, with enhanced sensitivity and selectivity.[16−19]

A wide range of magnetic sensors, such as anisotropic magnetoresistance, giant magnetoresistance, tunneling magnetoresistance, the Hall effect, and magnetoimpedance (MI) sensors are now available. Among them, sensors based on the MI effect have been considered as an effect element with higher field sensitivity and appropriate signal intensity for magnetic sensing purposes.[20−22] The MI effect is defined as the change of the electrical impedance of a conducting ferromagnetic (FM) with high transverse magnetic permeability (μ_t) in the presence of a static magnetic field.[23−29] By applying an external magnetic field, the skin depth (δ) changes due to the change in μ_t, thus varying the impedance of the FM element. In the case of the ribbon, with width w and length L, the impedance is approximately

$$Z = (1 - i)\frac{\rho L}{2w\delta} = \frac{(1 - i)L}{2w}(\pi\rho f\mu_t)^{1/2} \quad (1)$$

where ρ is electric resistivity, f is frequency of the current, and i = imaginary unit. Therefore, the impedance of the ribbon is a function of frequency, driving current, and the external dc

Received: August 3, 2019
Accepted: November 20, 2019
Published: November 20, 2019

DOI: 10.1021/acsaelm.9b00485
ACS Appl. Electron. Mater. XXXX, XXX, XXX−XXX

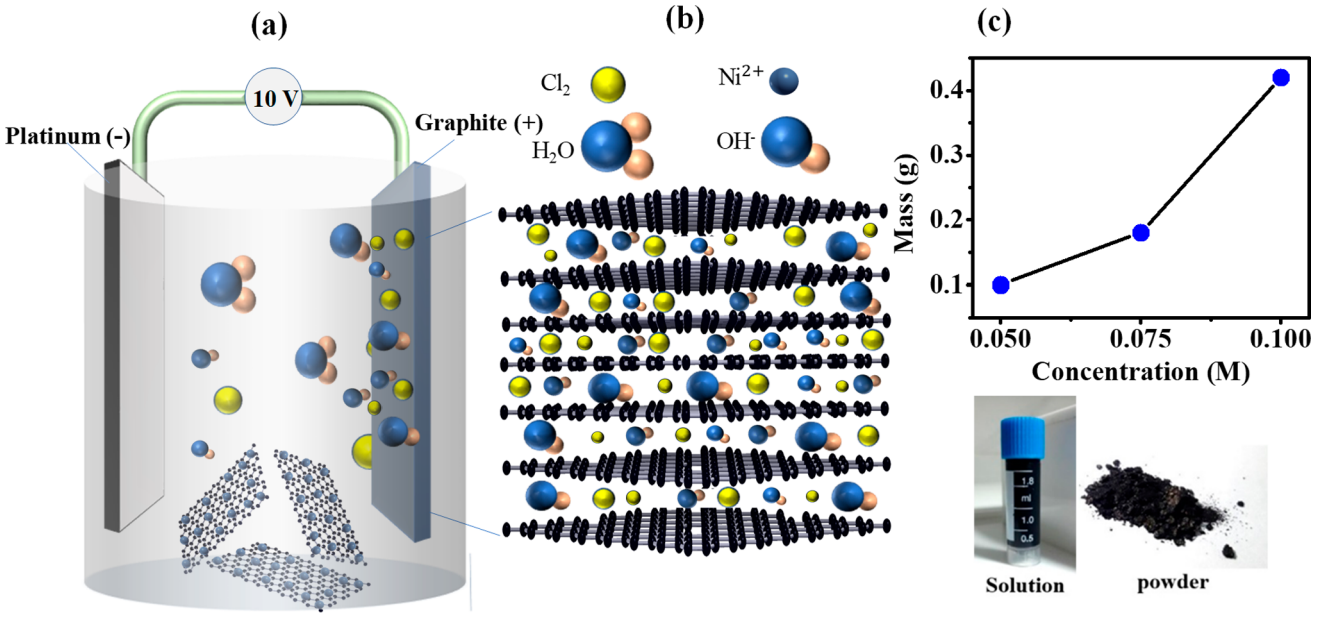

Figure 1. (a) Schematic of the proposed mechanism when magnetic Gr/Ni is produced. (b) The position of OH^- and Cl^- ions is illustrated between graphite sheets. These ions increase the interlayer distance of the graphite. Then, the Cl gas is produced and can exert an excessive force to separate graphite layers. Then, the distributed Gr sheets in the solution can trap Ni^{2+} ions. (c) Concentration of electrolyte solution and final mass of magnetic Gr/Ni composite.

magnetic field (H_{dc}) through μ_t and δ. The environmental sensing ability and improving the magnetic field sensor performance are two aspects of this phenomenon. Enhancement of magnetic field sensitivity has been reported by coating layers with different magnetization and conductivities on the surface of MI sensors.[28,30−34] The physical origins are well-known through the magnetic proximity effect,[8] decrease of surface roughness, and magnetic exchange interactions between sensors and coated magnetic layers. Also, surface modification of the ribbons has been reported intensively for detection of environmental elements through magnetic and nonmagnetic interactions with the environment.[21]

Recently, we applied electrochemical exfoliation of Gr using a solution containing Ni ions which leads to simultaneous exfoliation of Gr and deposition of Ni between Gr sheets.[15] Here, we extend this method toward fabrication of composites with controllable magnetic properties and introduce a useful technological application of such magnetic Gr/Ni composites. We investigate the application of such a composite in MI sensors with an observed enhanced ratio and sensitivity when coated atop an MI sensor.

In order to obtain a comprehensive study and achieve a physical description behind the experimental results, we proposed an electrodynamic model to explain the MI behavior in the studied structure. Our model is based on solving the linearized Maxwell equations for the electromagnetic fields coupled with the Landau−Lifshitz−Gilbert (LLG) equation for the magnetization dynamics of the sensor. These results can be used in interpreting the experimental results of our designed MI sensors. Both theoretical predictions and experimental observations confirm the MI response changes due to coating of magnetic composites with different magnetization strengths qualitatively. The fundamental physical phenomenon described in this work can be used for the development of magnetic field and environmental sensors based on the MI effect.

2. EXPERIMENTAL SECTION

2.1. Preparation of Gr/Ni Composite by Electrochemical Exfoliation. We used a two-electrode system for electrochemical exfoliation of graphite. Platinized silicon (100 nm thickness and lateral dimension of 0.5 × 10 cm^2) was used as the cathode electrode. Also, a graphite foil (2 × 10 cm^2) was used as the anode.[15] The distance between the two electrodes was kept constant at 2.8 cm. Electrolyte solutions were prepared by dissolving $NiCl_2{\cdot}6H_2O$ powder in water with three different molar ratios of 0.05, 0.075, and 0.1. A constant voltage (+10 V) was applied to the electrodes to provide expansion, exfoliation of graphite, and deposition of Ni. The voltage was maintained constant for 20 min to complete the exfoliation/deposition process. Afterward, the product was collected using vacuum filtration and repeatedly washed with deionized (DI) water. The resulted product was dispersed in water for sonication.

The mechanism of electrochemical exfoliation is depicted in Figure 1a,b. For an explanation of the exfoliation/deposition mechanism, see previous reports.[15,35] Reported processes are confirmed by the effect of initial $NiCl_2$/water concentration on exfoliation, as depicted in Figure 1c. In this figure, adding $NiCl_2$ results in higher production of Gr sheets, but below and above these values, final products do not show magnetic properties. Because OH^- and Cl^- are responsible for the production of Gr flakes, therefore the increasing molarity of $NiCl_2$ results in more exfoliated production content. As we are mainly interested in magnetic properties of our final products, we therefore investigate all of our samples made with 0.05, 0.075, and 0.1 M. Continuing, we represent a comprehensive study of products; investigate their conductivity, magnetization, and MI measurements; and discuss the mechanism of MI theoretically.

2.2. Characterization. The crystalline structure of samples was characterized using an X-ray diffractometer (XRD) with Cu Kα (λ = 0.154 nm) radiation. Fourier transform infrared (FTIR) spectra were recorded via a Bruker (Tensor 27) FTIR spectrometer with resolution of 1 cm^{-1} in transmission mode at room temperature. X-ray photoelectron spectroscopy (XPS) was done in an ESCA/AES system equipped with a concentric hemispherical analyzer (CHA, Specs model EA10 plus). The size and morphology of elements were observed by tunneling electron microscopy (TEM-Philips model CM120). Room temperature magnetization measurements were done via a vibrating sample magnetometer (Meghnatis Daghigh Kavir Co.).

DOI: 10.1021/acsaelm.9b00485
ACS Appl. Electron. Mater. XXXX, XXX, XXX−XXX

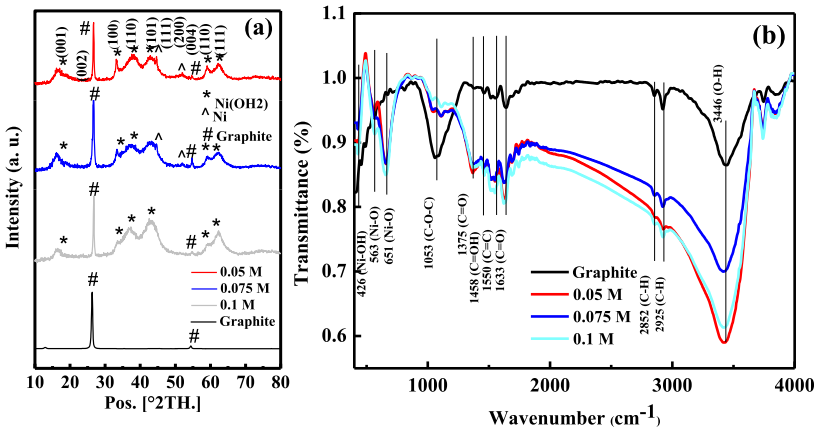

Figure 2. (a) X-ray diffraction (XRD) and (b) FTIR spectra of 0.1, 0.075, and 0.05 M samples and graphite foil.

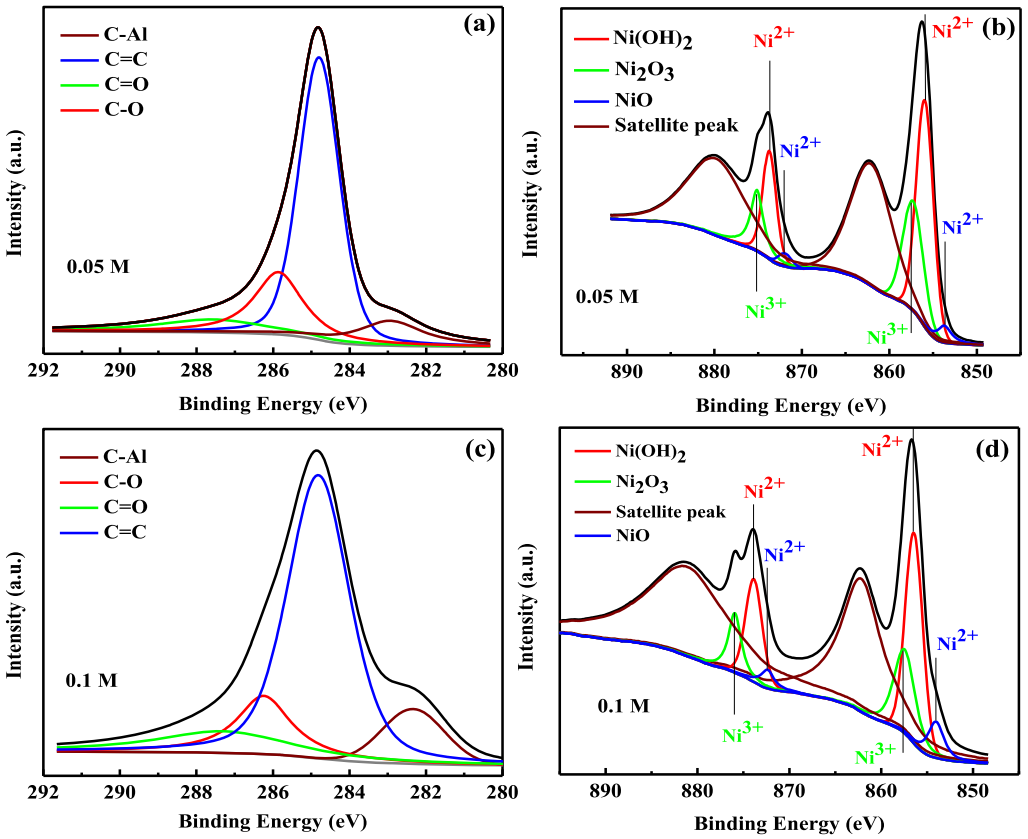

Figure 3. High-resolution XPS spectra of C 1s and Ni 2p core level of Gr/Ni sample of (a, b) 0.05 M and (c, d) 0.1 M.

Current−voltage (I−V) measurements were done by a two-probe method using a Keithley (model 2450) sourcemeter. Field emission scanning electron microscopy (FESEM) for samples was done by a VEGA TESCAN instrument.

2.3. Magnetoimpedance (MI) Measurement. The conventional melt-spinning technique is used for the preparation of amorphous Co-based ribbons, $Co_{68.15}Fe_{4.35}Si_{12.5}B_{15}$ (1 mm width, 40 mm length, and ∼20 μm thickness). The Gr/Ni composite with different molarities of 0.05, 0.075, and 0.1 M of $NiCl_2$ was drop-coated on the two surface sides of the ribbon at room temperature. Evaporation of water and nanoparticle solution was required before the data acquisition process started. An external magnetic field was produced by a solenoid and applied along the ribbon axis to measure the MI response of the samples by the four-point probe method. Different frequencies of ac current were supplied to the longitudinal direction of the ribbon by a function generator (GPS-2125), with a 50 Ω resistor in the circuit. The impedance was measured using the voltage and current across the sample using a digital oscilloscope (GPS-1102B). The MI ratio is defined as

$$\mathrm{MI}\% = \frac{Z(H_e) - Z(H_{e_{max}})}{Z(H_{e_{max}})} \times 100 \quad (2)$$

where Z refers to the impedance as a function of the external field H_e. The $H_{e_{max}}$ is the maximum field applied to the samples during the MI measurement. The longitudinal direction of samples was perpendicular to the Earth's magnetic field to minimize its effect on the MI response of samples.

DOI: 10.1021/acsaelm.9b00485
ACS Appl. Electron. Mater. XXXX, XXX, XXX−XXX

Table 1. Fitted XPS Data for fwhm and Peak Positions for C 1s and Ni 2p Core Level of 0.05 and 0.1 M Gr/Ni Sample

	C 1s (C—Al)		C 1s (C═C)		C 1s (C—O/C—Cl)		C 1s (C═O)	
sample	B.E. (eV)	fwhm (eV)	B.E. (eV)	fwhm (eV)	B.E. (eV)	fwhm (eV)	B.E. (eV)	fwhm (eV)
0.05 M	282.5	2	284.8	1.3	285.9	1.7	287.6	4.1
0.1 M	282.6	2.6	284.8	1.6	285.7	1.7	287.3	4.1
	Ni $2p_{3/2}$ (Ni^{2+})		Ni $2p_{3/2}$ (Ni^{3+})		Ni $2p_{1/2}$ (Ni^{2+})		Ni $2p_{1/2}$ (Ni^{3+})	
sample	B.E. (eV)	fwhm (eV)	B.E. (eV)	fwhm (eV)	B.E. (eV)	fwhm (eV)	B.E. (eV)	fwhm (eV)
0.05 M	855.9−853.7	2.3−1.9	857.4	2.7	873.6−871.9	1.8−1.9	875.1	1.7
0.1 M	856.4−854	2.3−2	857.4	2.7	873.9−872.4	2.2−1.8	875.9	1.6

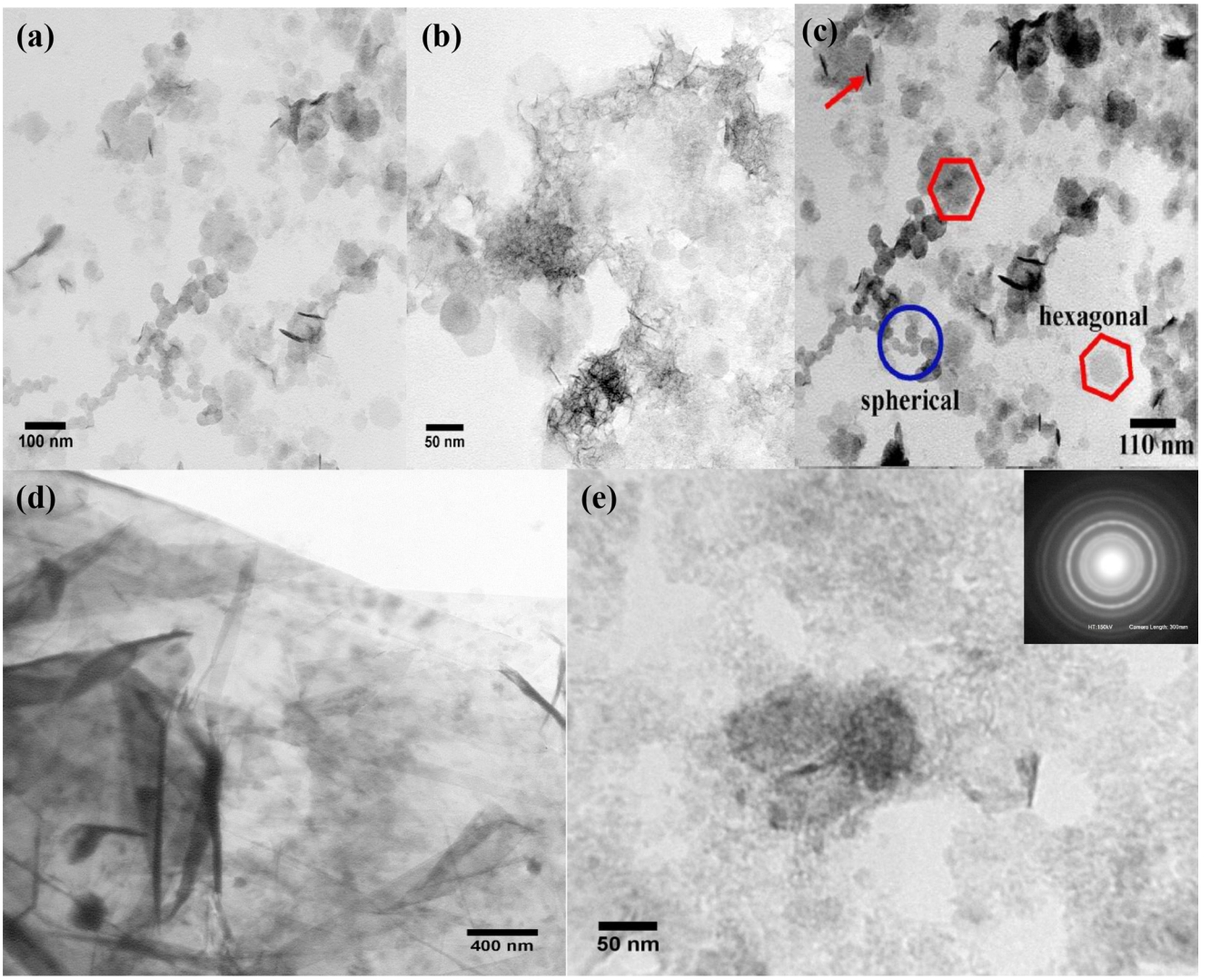

Figure 4. TEM images of (a) 0.1 M, (b) 0.075 M, and (c) 0.05 M samples and (d) the micron boundary size of Gr sheets. (e) SAED pattern of the 0.05 M sample.

3. RESULTS AND DISCUSSION

XRD analysis was employed to confirm the crystalline structures of Gr/Ni composites as shown in Figure 2a. The dominant diffraction peak of the initial graphite foil at 2θ = 26.31° indicates an interlayer d-spacing of 3.38 Å, while in the final samples the (002) diffraction peak appeared at 26.16° with an interlayer d-spacing of 3.40 Å. There are some diffraction peaks that belong to $Ni(OH)_2$. One broad diffraction peak at around 2θ = 13.45° and another one at 2θ = 33.2° represent the (001) and (100) planes of the β-phase, respectively (JCPDS 001-1047), while (110) and (111) planes of the α-phase appear with a broad diffraction peak at 2θ = 36−39.3° (JCPDS 06-0075).[36] Other two diffraction peaks with 2θ = 59° and 62.1° represent (110) and (111) planes of β-phase $Ni(OH)_2$. The diffraction peaks for Ni were also observed at 2θ = 44.6° and 52° which correspond to (111) and (200) planes, respectively (JCPDS 001-1260), indicating the presence of face-centered cubic (fcc) Ni with a lattice constant of 3.51 Å. By increasing the concentration of $NiCl_2$, the less relative intensity of Ni peaks can be seen. The Scherrer equation is used to calculate the average size of the deposited Ni and $Ni(OH)_2$ crystals. The average sizes were

DOI: 10.1021/acsaelm.9b00485
ACS Appl. Electron. Mater. XXXX, XXX, XXX−XXX

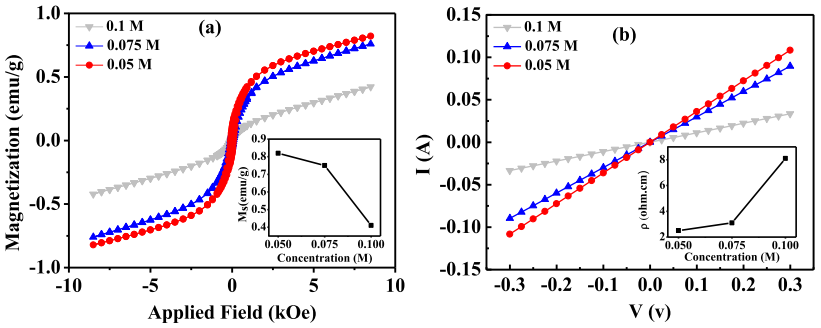

Figure 5. (a) VSM magnetization plots of 0.05, 0.075, and 0.1 M samples. The inset shows the saturation magnetization of samples versus concentration. (b) Current−voltage (I−V) curve measurement for 0.05, 0.075, and 0.1 M samples, and the inset shows the resistivity (ρ) of samples versus concentration.

found to be 43 and 32 nm, respectively. Also, TEM images, explained later, proved the observed sized.

To elucidate the interaction of Ni nanoparticles (Ni NPs) with the Gr sheets, FTIR spectra were recorded and analyzed. FTIR is a useful technique to confirm that the NPs are anchored on the Gr surface, as shown by several groups.[37,38] Figure 2b shows the FTIR spectra of the graphite foil and produced samples. It shows a number of oxygen functionalities due to the presence of residual elements in the Gr.[39] The absorption peaks at ∼1633, ∼1550, and ∼1375 cm^{-1} should be assigned to stretching vibrations (υ) of C═O. The presence of O—H is confirmed by the strong and broad band at 3446 cm^{-1}. The intensity of this peak is stronger for the synthesized Gr/Ni structures than the initial graphite foil which shows the effect of the aqueous solution of the experiment on generation of hydroxyl elements. The absorption peak at 1053 cm^{-1} should be attributed to stretching vibrations (υ) of C—O—C[40] that disappear after exfoliation. The bands at 2925 and 2852 cm^{-1} are assigned to the asymmetric and symmetric vibrations of C—H, respectively.[41,42] Comparing the FTIR spectra of graphite foil with the final sample, the spectrum of Gr/Ni structures clearly exhibits a considerable red-shift (particularly to the major vibration of C═C and —OH bonds), which may be because of the Ni NPs bonding to the Gr layers.[43] The absorption bands at 651, 563, and 426 cm^{-1} are attributed to the NiO and n(Ni—OH) vibration.[43]

High-resolution XPS spectra are used to probe the chemical compositions of the 0.05 and 0.1 M Gr/Ni composites (Figure 3a−d). Peak positions and fwhm values are presented in Table 1. The presence of $Ni(OH)_2$ and Ni-oxides is observed using Ni 2p peaks, while no Ni is observed. However, Ni peaks were observed in the XRD measurements which reconfirms the presence of Ni compounds. This contradiction is expected as the XPS is able to probe the surface of the materials only. Also, rather than the oxides at the surface of the Ni, there are other compounds that prevent Ni signatures from showing up.

The area ratios allow calculating the relative proportions of atoms in each binding for a given element. The concentration ratio of Ni:C was estimated using the following relation for 0.05 and 0.1 M samples:

$$\frac{C_{Ni}}{C_C} = \frac{I_{Ni}}{S_{Ni}} \times \frac{S_C}{I_C} \quad (3)$$

where C, I, and S are the elemental concentrations, XPS peak area, and corresponding sensitivity factors. The relative surface ratio of $\frac{C_{Ni}}{C_C}$ for the 0.1 M sample is 0.36 which increases to 0.51 for the 0.05 M sample. Also $\frac{C_{Ni}}{C_O}$ for the 0.1 M sample is 0.71 which increases to 0.85 for the 0.05 M sample, and $\frac{C_C}{C_O}$ for the 0.05 M sample is 1.66 and increases to 1.93 for the 0.1 M sample.

TEM images of samples are shown in Figure 4. Hexagonal structures appear in Figure 4a−c that are presumed to be related to $Ni(OH)_2$ nanocrystals, whose crystallization at the β-hexagonal phase was identified from our XRD data. Thes Ni-based nanocrystals are separated by dashed lines in Figure 4c. They have also different alignments/geometry, e.g., rolled up structures, which are shown by an arrow in Figure 4c that appears with more probability in samples made with higher molarities, i.e., 0.1 M sample. Results dictate a small thickness of the crystal, because they look to have thin planar geometry. In Figure 4b,d we see crumpled Gr and nanocrystals sticking to it for the 0.75 M sample. The nanocrystals (Ni-oxides, Ni, $Ni(OH)_2$) appear to be randomly distributed on Gr sheets, and this character is supposed to be the reason of their superparamagnetic-like response (presented later).[15] TEM results confirm the size of Ni-based nanocrystals obtained by XRD data. The brightness of Gr sheets appearing in this image confirms their small thickness. The image in Figure 4d shows micron-sized formation of Gr sheets which is in agreement with dynamic light scattering (DLS) results with a determined particle size of 1.2 μm. The selected area electron diffraction (SAED) pattern in Figure 4e, measured for randomly selected Gr sheets of the 0.05 M sample, represents the polycrystalline nature of the Gr.

To investigate the effect of the molarity of $NiCl_2$ on the magnetic properties of the Gr/Ni composite, the magnetic hysteresis loops of the 0.05, 0.075, and 0.1 M samples were recorded at room temperature. The VSM results shown in Figure 5a represent the superparamagnetic-like response of the samples. By decreasing the molarity of $NiCl_2$, the magnetization of the composite increases (see the inset of Figure 5a). XRD results showed the lower concentration of Ni in samples synthesized by higher $NiCl_2$ molarities. The formation of Ni or $Ni(OH)_2$ depends on the concentration of OH^- at the cathode. This means that increasing the molarity of $NiCl_2$ results in the increasing generation rate of OH^- and therefore the production ratio of $Ni(OH)_2$ with respect to the Ni would increase. Consequently, by controlling the molarity of the solution, the concentration of FM Ni and thus the magnetization will be controlled. The XPS results are compared with magnetization which indicates that the concentration of Ni to $Ni(OH)_2$ is more in the 0.05 M sample and caused a higher

DOI: 10.1021/acsaelm.9b00485
ACS Appl. Electron. Mater. XXXX, XXX, XXX−XXX

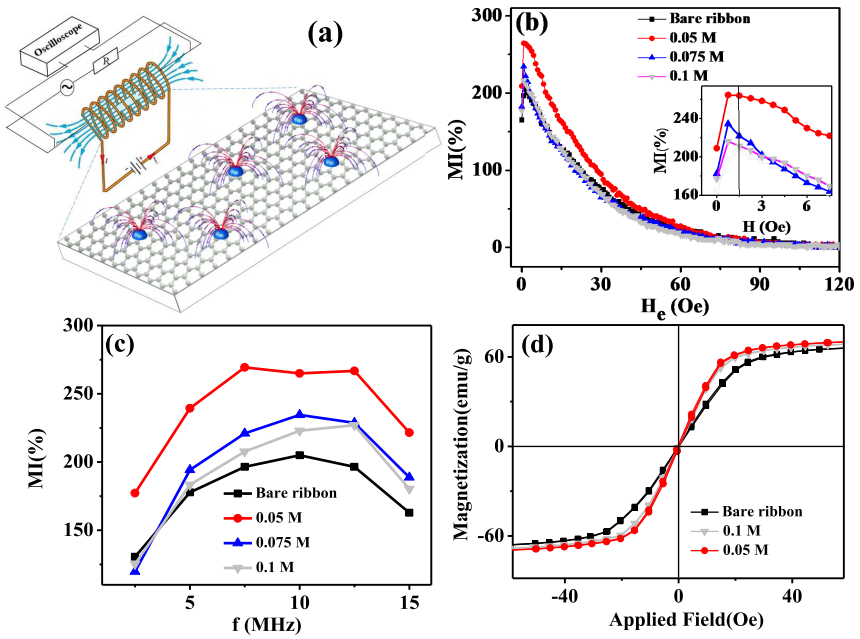

Figure 6. (a) Schematic illustration of the measurement setup for the MI response and the structural conditions in the MI sensor when the ribbon is coated with Gr/Ni composites. The influence of the Gr/Ni layer on the MI is related to stray fields induced by magnetic Ni NPs. The stray fields change the magnetization distribution in the magnetic ribbon and affect the permeability and the MI effect. (b) MI ratio as a function of applied magnetic field for the bare ribbon and ribbon drop-coated by Gr/Ni NPs with three different molar ratios. The inset shows an enlarged portion of the low-field MI curves. (c) Frequency dependence of the impedance response of all samples. (d) Magnetic hysteresis loops of the bare ribbon and ribbon drop-coated by Gr/Ni composite with molar ratios of 0.05 and 0.1.

magnetization. This also confirms that the conductivity of the 0.05 M sample is more than that of the 0.1 M sample which has been seen by our $I-V$ experiment. For $I-V$ measurements, silver paste-coated pellets connecting wire were used. $I-V$ plots are linear, showing conductive behavior of all samples (Figure 5b). Resistivity of samples was determined by the linear fitting of $I-V$ plots. Resistivity increases from the 0.05 M sample to the 0.1 M sample which is shown in the inset of Figure 5b. According to the aforementioned growth mechanism, we can interpret that as the molarity of $NiCl_2$ in solution increases, there is more OH^- generation on the cathode and more hydroxide elements in Gr that result in more resistivity in samples. XPS and XRD data show more hydroxide densities and lower Ni elements for samples prepared from solutions with higher molarities of $NiCl_2$.

3.1. Magnetic Gr/Ni Detection by Magnetoimpedance Measurement: Testing of the Biosensor. In the biosensor sector, the detection of functionalized magnetic NPs has become a current active research issue.[22,44] Besides high sensitivities, the NP detector should also have low power consumption, small size, quick response, stability of operation parameters, resistance against aggressive medium, and low cost. Different sensing techniques are employed for the NP detection: anisotropic magnetoresistance,[45] giant magnetoresistance,[46,47] and magnetoimpedance (MI)[48,49] effects; in the following, we try to improve the sensitivity of the later one using our Gr/Ni composites.

To evaluate the potential applications in sensing devices, we study the MI magnetic field and frequency dependence for a Co-based FM ribbon and later try to determine the effect of the stray fields introduced by the magnetic Gr/Ni NPs on the MI response. By applying an ac charge current with frequency f to the samples, we investigate how the impedance of the ribbon changes as a function of the external magnetic field. We perform field sweep impedance measurements at the frequency of f = 10 MHz (frequency where maximum MI was already determined) for ribbon (as-cast) and ribbon drop-coated by Gr/Ni NPs with three different molar ratios of 0.05, 0.075, and 0.1. The schematic illustration of the measurement setup for the MI response and the structural features of the MI-based sensor is presented in Figure 6a. As determined above, the lower the molarity of the samples, the higher the content of the Ni in the sample. Each of the Ni NPs can produce a stray field on the surface of the ribbon and thereby affect the magnetic anisotropy and permeability of the ribbon. As can be seen from Figure 6b, the MI ratio for the bare ribbon has the smallest value and increases for the drop-coated samples. The maximum values of the MI ratio are 201%, 218%, 238%, and 275% for the bare ribbon and the ribbon with the drop-coated Gr/Ni composite with molar ratios of 0.1, 0.075, and 0.05, respectively. The inset of Figure 6b shows an enlarged plot of the low-field MI curves. One can see that the anisotropy field is 1.5 Oe for the bare ribbon, while for the drop-coated sample, the amount of the anisotropy field decreases and reaches 1 Oe. When the Ni NPs are affected by the external field, they can produce a measurable stray field. As a result, the presence of the Gr/Ni composite leads to a sizable increase in the MI ratio near the anisotropy field and the displacement of the MI curve. This finding is of practical importance, as the Gr/Ni composite can be better used as a magnetic biomarker for applications in medical diagnosis, especially in the cases in which Gr plays the role of biomarking.[50] Also, compared to the reported sensitivities in the literature[21,51] the sensitivity of our sample may be much lower, but in using a biocompatible Gr-based material,[10,14,17,18] our sample would show a valuable advantage.

In order to evaluate the difference between the MI ratio of the bare ribbon and Gr/Ni composite-covered ribbon, we measured the MI at different frequencies ranging from 1 to 15

DOI: 10.1021/acsaelm.9b00485
ACS Appl. Electron. Mater. XXXX, XXX, XXX−XXX

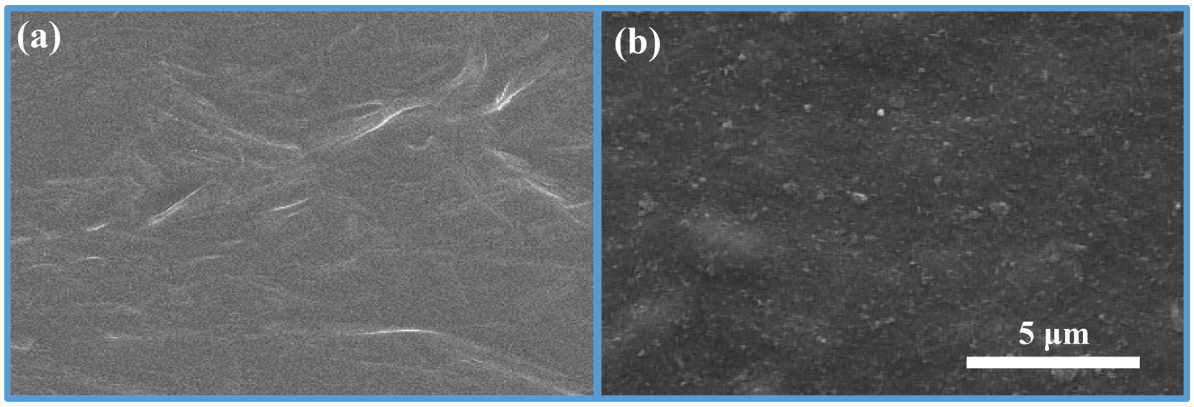

Figure 7. Field emission scanning electron microscopy (FESEM) images of (a) the bare ribbon and (b) ribbon drop-coated by Gr/Ni nanocomposite with molar ratios of 0.05.

MHz. The maximum MI ratio of all samples versus frequency is plotted in Figure 6c. It is observed in Figure 6c that, for the samples, by increasing the frequency, the maximum MI ratio increases initially, reaches a maximum at f = 10 MHz, and then decreases for higher frequencies. This trend is interpreted by considering the relative contributions of moment rotation and domain wall (DW) motion, as both contribute to the transverse magnetic permeability and hence the MI response.[20,23,51] Note that when frequency increases well above 100 kHz, the contribution of DW motion would be damped because the presence of eddy current and moment rotation becomes dominant.[20] Therefore, the MI ratio decreases at high frequencies.

Finally, to investigate the effect of the drop-coated Gr/Ni composite on the magnetic properties of the ribbons, the conventional VSM method was used to obtain the magnetic hysteresis loops. Figure 6d shows the magnetic hysteresis loops of the bare ribbon and ribbon drop-coated by Gr/Ni composite with molar ratios of 0.05 and 0.1. All the loops are thin and narrow, and magnetization is saturated at a small applied field, which shows their soft FM characteristics. According to Figure 6d, after coating, the saturation field decreases, and the differential magnetic permeability of the sample which is proportional to the magnetization slope has increased dictating a weak field-sensitive and magnetically softer state. As mentioned before, the MI effect is a highly surface-sensitive phenomenon due to the low skin depth of the ribbon. In this context, there are many reports on the surface modification of MI sensors by coating layers with different magnetization and conductivities.[31−33,52−54] All articles have reported the increase in the MI ratio, and the physical origins are well-discussed through the decrease of surface roughness and the closed magnetic flux path[31−33] and magnetic exchange interactions between sensors and coated magnetic layers.[52,53] Also, some reports have used Gr-based materials and reported the better performances of their sensor device.[8,28,55−59] For example, the vertical Gr sheets may redistribute the surface magnetic field, which is good for improving the transverse permeability,[57] or the $MnFe_2O_4$−Gr oxide nanocomposite increased the MI ratio due to the suppressed physical motion of the $MnFe_2O_4$ NPs on the Gr sheet, as well as the enhanced effective anisotropy of the sample.[56] Very recently, we coated the (Gr nanoplates)/(yttrium iron garnet) (GNPs/YIG) composite on a magnetic ribbon and showed that the proximity-induced magnetism (PIM) in Gr adjacent to magnetic YIG influences the magnetization of the GNPs to make them a wholly magnetized plane.[8] Such a magnetized plane can be mounted on the surface of ribbon MI sensors, and thereby the MI response is enhanced against the external applied magnetic field significantly. However, in the case of Gr/Ni composite, the difference in the magnetization of composites is related to the difference in the amount of magnetic particles in the composite and not only PIM. The 0.05 M sample has a higher impact on diminishing the magnetic flux at the surface of the MI element due to higher magnetization than other samples. Another reason for the increase in the MI ratio can be attributed to the decrease of the surface roughness. To see the effect of coating on the roughness of the ribbon we used FESEM images of the surface. Images of the free side of the bare ribbon and Gr/Ni-coated ribbon are presented in Figure 7a,b, respectively. As observed, the roughness has decreased due to a surface coverage of unevenness at the surface by the Gr/Ni composite layer. This fact is in agreement with the increase of the MI ratio because such a coating decreased the undesired emanating field at the surface. The following electromagnetic model is presented to understand the observed results.

4. MODEL FOR IMPEDANCE OF RIBBON/[GR/NI] STRUCTURES

In this section we describe a model for the MI response of the ribbon/[Gr/Ni] structures. MI response can be found by solving the Maxwell equations for the electromagnetic fields and the Landau−Lifshitz−Gilbert (LLG) equation for the magnetization dynamics by considering the boundary conditions at the interfaces of the system. The changes caused by the Gr/Ni layer on the MI response are related to stray fields which magnetic Ni NPs induce. The magnetization distribution can be tuned by the stray fields and affect the permeability and therefore the MI effect. One assumption is that the Gr/Ni layer generates a spatially uniform effective field H_s on the ribbon surface.[22] Therefore, we are able to describe qualitatively the influence of stray fields on the MI response. The value of H_s is assumed to be proportional to the concentration of MNPs in the Gr/Ni sample, because the Gr/Ni saturation magnetization increases linearly (see Figure 5a) with the concentration of NPs. Also, we assume that the values of the permeability in the magnetic layer are determined by the magnetization rotation only because the DW motion is strongly damped at sufficiently high frequencies (above 100 kHz).[20]

DOI: 10.1021/acsaelm.9b00485
ACS Appl. Electron. Mater. XXXX, XXX, XXX−XXX

A schematic of the ribbon/[Gr/Ni] structures and the coordinate system used for the analysis is shown in Figure 8.

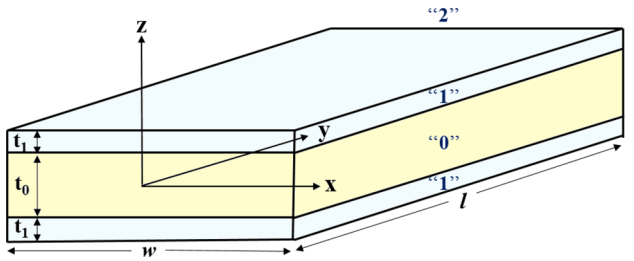

Figure 8. Schematic of the ribbon/[Gr/Ni] structures and the coordinate system.

There are three regions 0, 1, and 2 denoting the magnetic ribbon layer, the Gr/Ni layer, and air. The film structure has length l and width $w < l$ and consists of thickness t_0 and t_1 for the ribbon and Gr/Ni layer, respectively. The structure is subjected to an alternating driving field $E = E_0 e^{-iwt}$, and an external magnetic field H_e is parallel to the long side of the sample (y-axis). It is assumed that the film length and width are much larger than its thickness. Introducing the scalar and vector potentials, φ and $\boldsymbol{A}$, Maxwell's equations can be expressed as ($\nabla \cdot \boldsymbol{A} = 0$ is used)

$$\nabla^2 \boldsymbol{A}_j(r, t) = \mu_j \sigma_j \left[\nabla \varphi_j(r, t) + \frac{\mathrm{d}}{\mathrm{d}t} \boldsymbol{A}_j(r, t) \right]$$

$$\nabla^2 \varphi_j(r, t) = 0 \tag{4}$$

where $j = 0, 1$ corresponds to regions 0 and 1, and σ_j and μ_j correspond to conductivity and permeability of the magnetic ribbon for $j = 0$ and Gr/Ni layer for $j = 1$. The general solutions for the vector potential in the three regions can be expressed as[52]

$$A_0 = \frac{iE_0}{\omega}[B_0 \cosh(\alpha_0 z) + C_0 \sinh(\alpha_0 z) - 1] \tag{5}$$

$$A_1 = \frac{iE_0}{\omega}[B_1 \cosh(\alpha_1 z) + C_1 \sinh(\alpha_1 z) - 1] \tag{6}$$

$$A_2 = \frac{iE_0}{\omega} B_2 \left[\frac{l}{w} \ln\left(\frac{r + w}{r - w}\right) - \frac{2z}{w} \arctan\left(\frac{w}{2y} \frac{l}{r}\right) + \ln\left(\frac{l + r}{\sqrt{w^2 + 4z^2}}\right) \right] \tag{7}$$

where, $r = (w^2 + 4z^2 + l^2)^{1/2}$, $\alpha_k = (1 + \mathrm{i})\left(\frac{\omega \mu_j \sigma_j}{2}\right)^{1/2}$ and due to symmetry along the Z axis, $A_0(Z) = A_0(-Z)$, the constant of C_0 is zero. The boundary conditions allow one to find the constants B_0, B_1, C_1, and B_2 in eqs 5−7 and describe completely the distribution of the vector potential (see the Appendix). When the potential distribution is obtained, because the magnitude of the driving electric field is constant, the impedance can be obtained as the proportionality factor between the voltage and the total current in the device where

$$Z = \frac{lE_0}{2w} \left(\int_0^{t_0/2} J_0(z)\, \mathrm{d}z + \int_{t_0/2}^{t_0/2 + t_1} J_1(z)\, \mathrm{d}z \right)^{-1} \tag{8}$$

where

$$J_0 = E_0 \sigma_0 B_0 \cosh(\alpha_0 z) \tag{9}$$

$$J_1 = E_0 \sigma_1 [B_1 \cosh(\alpha_1 z) + C_1 \sinh(\alpha_1 z)] \tag{10}$$

Finally, we obtain the impedance Z of the film with the Gr/Ni layer:

$$Z = \frac{l}{2w} \frac{1}{\gamma'} \left[\cosh\left(\frac{\alpha_1 t_0}{2}\right) \cosh(\alpha_1 t) \left[\left(\tanh(\alpha_1 t) - \tanh\left(\frac{\alpha_1 t_0}{2}\right) \right) \left(\gamma + \beta\gamma' \tanh\left(\frac{\alpha_0 t_0}{2}\right) \right) + \left(1 - \tanh\left(\frac{\alpha_1 t_0}{2}\right) \tanh(\alpha_1 t) \right) \left(\gamma' + \beta\gamma \tanh\left(\frac{\alpha_0 t_0}{2}\right) \right) \right] \right] / \left[\frac{2\sigma_0}{\alpha_0} \tanh\left(\alpha_0 \frac{t_0}{2}\right) + \frac{2\sigma_1}{\alpha_1} \left[\sinh(\alpha_1 t_1) + \beta \tanh\left(\frac{\alpha_0 t_0}{2}\right) \cosh(\alpha_1 t_1) - \beta \tanh\left(\frac{\alpha_0 t_0}{2}\right) \right] \right] \tag{11}$$

Here, $t = \frac{t_0}{2} + t_1$, $\gamma = 1 + \ln\frac{2l}{w}$, $\gamma' = \frac{\pi}{w} \frac{\mu_1}{\mu_2 \alpha_1}$, and $\beta = \left(\frac{\mu_1 \sigma_0}{\mu_0 \sigma_1}\right)^{1/2}$.

4.1. Effect of the Gr/Ni Layer on Ribbon Permeability.

The MI response of the ribbon is controlled by the transverse magnetic permeability. Transverse magnetic permeability depends on factors like anisotropy distribution, domain structure, mode of the magnetization variation, and so on. Since in the experiment the current frequencies are sufficiently high, the value of the transverse permeability in the FM layers occurs because of the magnetization rotation of the ribbon. Validation of this approximation is at sufficiently high frequencies (>100 kHz) when the DW motion is damped.[20] Also, the anisotropy is considered to be in the plane of the ribbon.

By minimizing the free energy one can find the magnetization distribution in the FM layers. Taking into account the effective stray field, H_s, the minimization procedure results in the following equation for the equilibrium magnetization angle, θ:

$$H_a \sin(\theta - \psi) \cos(\theta - \psi) - H_s \sin(\theta - \varphi) - H_e \cos\theta = 0 \tag{12}$$

Here, H_a is the anisotropy field in the FM layers, and ψ is the deviation angle of the anisotropy axis from the transverse direction.

In the magnetic susceptibility model, magnetization dynamics is governed by the LLG equation and is given by

$$\frac{\partial \boldsymbol{m}}{\partial t} = -\gamma \boldsymbol{m} \times \boldsymbol{H}_{\mathrm{eff}} + \alpha \boldsymbol{m} \times \frac{\partial \boldsymbol{m}}{\partial t} \tag{13}$$

where $\boldsymbol{m}$ is vector magnetization, $\boldsymbol{H}_{\mathrm{eff}}$ is the effective field, γ is the electron gyromagnetic ratio, and α is the Gilbert damping constant. The solution of the linearized LLG equation results in the following expression for the transverse permeability in the ribbon layer:[53]

$$\mu_0 = 1 + \frac{\omega_m[\omega_m + \omega_1 - i\alpha\omega] \sin^2\theta}{[\omega_m + \omega_1 - i\alpha\omega][\omega_2 - i\alpha\omega] - \omega^2} \tag{14}$$

Here, $\omega_m = 4\pi\gamma M_s$, M_s is the saturation magnetization of the ribbon, $\omega = 2\pi f$ is the angular frequency, and

$$\omega_1 = \gamma[H_a \cos^2(\theta - \psi) - H_s \cos(\theta - \varphi) + H_e \sin\theta] \tag{15}$$

DOI: 10.1021/acsaelm.9b00485
ACS Appl. Electron. Mater. XXXX, XXX, XXX−XXX

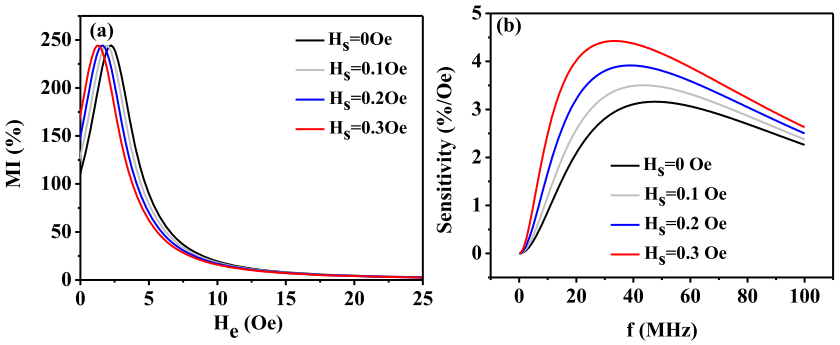

Figure 9. (a) Field dependence of the MI ratio $\Delta Z/Z$ calculated at $f = \frac{\omega}{2\pi} = 10$ MHz for the ribbon without the Gr/Ni layer and the ribbon with the Gr/Ni layer for different values of the effective stray field H_s. (b) Frequency dependence of the impedance sensitivity calculated by means of eq 17 for different values of H_s. Parameters used for calculations are $w = 8$ mm, $l = 4$ cm, $t_0 = 20$ μm, $t_1 = 10$ μm, $\sigma_0 = 5.81 \times 10^7$ $\frac{1}{\Omega m}$, $\sigma_1 = 10^3$ $\frac{1}{\Omega m}$, $M_s = 800$ Oe, $\theta = 0.75\pi$, $\varphi = -0.1\pi$, $\psi = 0.48\pi$, $\alpha = 0.1$, $H_a = 4$ Oe.

$$\omega_2 = \gamma[H_a \cos 2(\theta - \psi) - H_s \cos(\theta - \varphi) + H_e \sin\theta] \quad (16)$$

Thus, the MI response in the ribbon with a Gr/Ni layer can be calculated as follows. The first step is the determination of the transverse permeability in the FM layer by using eq 14. The second step is substitution of eq 14 into eq 11 and then the calculation of the impedance Z of the film with the Gr/Ni layer. When the impedance Z is determined, the MI response of the ribbon with the Gr/Ni layer can be obtained by means of eq 2.

4.2. MI Response of Ribbon/[Gr/Ni] Structures: A Comparison between the Experiment and Modeling.

Figure 9a shows the field dependence of the MI ratio calculated at 10 MHz for the ribbon without the Gr/Ni layer and the ribbon with the Gr/Ni layer considering different values for the effective stray field, H_s. Here, only results for the range of positive fields are presented because the MI ratio is symmetric with respect to the sign of the external field. When the concentration of the MNPs increases the saturation magnetization increases too, and in result the effective stray field increases. As a result, the MI ratio shifts toward low external fields with increasing H_s and exhibits a dependence similar to the one observed in the experiment.

For analyzing the variation of the MI effect, let us introduce the impedance field sensitivity, which is defined as follows:

$$S = \frac{|\Delta Z|}{|\Delta H_e|} = \frac{Z(H_e = -H_a) - Z(H_e = 0)}{H_a} \quad (17)$$

For different values of the effective stray field, H_s, Figure 9b represents the frequency dependence of the impedance sensitivity calculated by means of eq 17. At relatively low frequencies the field sensitivity increases and attains a peak at f = 20 MHz. The position of the highest sensitivity shifts to lower frequencies with a growth of the effective stray field, H_s.

The proposed model allows one to describe qualitatively the main features of the experimental results of the MI response of a ribbon coated with a Gr/Ni layer. However, some experimental results cannot be explained according to the model. It is demonstrated that the contribution of the stray fields induced by MNPs in the Gr/Ni layer leads to a shift toward low external fields with an increase of H_s. It should be noted that the model does not describe the essential increase of the MI response with an increase in the concentration of MNPs in the Gr/Ni layer. The disagreement between theoretical and experimental results may be attributed to the fact that, in the proposed model, the contribution of surface roughness was not considered. There are many experimental works that demonstrated the fact that reduction of roughness can lead to increase of the MI response.[27,28,31,33] Closure of magnetic flux paths due to surface modification of the ribbons is explained for the increase of the MI response. Also, in our model, it is shown that for the stray fields produced by the MNPs, H_s describes the effect of the Gr/Ni layer on the MI of the ribbon qualitatively. Here, for an exact calculation the amount of H_s should be gained with exact distributions through numerical solution.

5. CONCLUSION

In summary, the present study demonstrates that electrochemically exfoliated Gr is a promising method for fabricating magnetic Gr sheets/Ni nanocrystal composites in high quality. By changing the molarity of a $NiCl_2$ aqueous solution, different magnetic strengths of the final composite material were achieved. Different molarities of 0.05, 0.075, and 0.1 M of $NiCl_2$ for fabrication of the samples result in different magnetization of the material. The higher molarity results in lower magnetization. In addition to the focus on the novel fabrication of materials, we further investigate the application of the synthesized materials in MI sensors with an observed enhanced ratio and sensitivity when applied atop an MI sensor. The experimental observation of the MI response of our sensor shows higher MI% for the sensor coated with the Gr/Ni sample with a higher magnetization. By solving the linearized Maxwell equation and LLG equation for the magnetization dynamics we could find the origin of the observed MI behaviors under the presence of Gr/Ni composite. The results can be considered for future developments of MI-based sensors and biosensors.

APPENDIX

Boundary conditions require that A and $\frac{1}{\mu}\frac{dA}{dz}$ be continuous:

DOI: 10.1021/acsaelm.9b00485
ACS Appl. Electron. Mater. XXXX, XXX, XXX−XXX

$$\boldsymbol{A_0} = \boldsymbol{A_1} \qquad z = \frac{t_0}{2}$$

$$\mu_1 \frac{\mathrm{d}}{\mathrm{d}z}\boldsymbol{A_0} = \mu_0 \frac{\mathrm{d}}{\mathrm{d}z}\boldsymbol{A_1}$$

$$\boldsymbol{A_1} = \boldsymbol{A_2} \qquad z = \frac{t_0}{2} + t_1$$

$$\mu_2 \frac{\mathrm{d}}{\mathrm{d}z}\boldsymbol{A_1} = \mu_1 \frac{\mathrm{d}}{\mathrm{d}z}\boldsymbol{A_2} \tag{A1}$$

By substitution of eqs 5−7 into eq A1 with the approximation of $\boldsymbol{A}_2$ for $w \ll l$:

$$B_0 \cosh(x_0) - B_1 \cosh(y_0) - C_1 \sinh(y_0) = 0$$

$$B_0\beta \sinh(x_0) - B_1 \sinh(y_0) - C_1 \cosh(y_0) = 0$$

$$B_1 \cosh(z_0) + C_1 \sinh(z_0) - B_2\gamma = 1$$

$$B_1 \sinh(z_0) + C_1 \cosh(z_0) + B_2\gamma' = 0 \tag{A2}$$

where

$$x_0 = \frac{\alpha_0 t_0}{2} \qquad y_0 = \frac{\alpha_1 t_0}{2} \qquad z_0 = \alpha_1 t$$

$$t = \frac{t_0}{2} + t_1 \quad \gamma = 1 + \ln\frac{2l}{w} \quad \gamma' = \frac{\pi}{w}\frac{\mu_1}{\mu_2\alpha_1}$$

Solving for the coefficients, we obtain

$$B_0 = \frac{1}{E}$$

$$B_1 = \frac{1}{E}(\cosh(x_0)\cosh(y_0) - \beta \sinh(x_0)\sinh(y_0))$$

$$C_1 = \frac{1}{E}(\beta \sinh(x_0)\cosh(y_0) - \sinh(y_0)\cosh(x_0))$$

$$E = \frac{1}{\gamma'}\cosh(x_0)\cosh(y_0)\cosh(z_0)[(\tanh(z_0) - \tanh(y_0))(\gamma + \beta\gamma'\tanh(x_0)) + (1 - \tanh(y_0)\tanh(z_0))(\gamma' + \beta\gamma\tanh(x_0))] \tag{A3}$$

AUTHOR INFORMATION

Corresponding Authors

*E-mail: mrh.hajiali67@gmail.com.

*E-mail: m-mohseni@sbu.ac.ir.

ORCID

Mohammadreza Hajiali: 0000-0001-5068-4437

Seyed Majid Mohseni: 0000-0001-5626-533X

Author Contributions

The manuscript was written through contributions of all authors. All authors have given approval to the final version of the manuscript.

Notes

The authors declare no competing financial interest.

ACKNOWLEDGMENTS

Support from Iran National Science Foundation (INSF) is acknowledged.

REFERENCES

(1) Wang, Y.; Chen, X.; Zhong, Y.; Zhu, F.; Loh, K. P. Large Area, Continuous, Few-Layered Graphene as Anodes in Organic Photovoltaic Devices. *Appl. Phys. Lett.* **2009**, *95* (6), 063302.

(2) Bae, S.; Kim, H.; Lee, Y.; Xu, X.; Park, J.-S.; Zheng, Y.; Balakrishnan, J.; Lei, T.; Ri Kim, H.; Song, Y. I.; Kim, Y.-J.; Kim, K. S.; Özyilmaz, B.; Ahn, J.-H.; Hong, B. H.; Iijima, S. Roll-to-Roll Production of 30-Inch Graphene Films for Transparent Electrodes. *Nat. Nanotechnol.* **2010**, *5* (8), 574−578.

(3) Wu, Z.; Parvez, K.; Feng, X.; Müllen, K. Graphene-Based in-Plane Micro-Supercapacitors with High Power and Energy Densities. *Nat. Commun.* **2013**, *4* (1), 2487.

(4) Geim, A. K.; Novoselov, K. S. The Rise of Graphene. *Nat. Mater.* **2007**, *6* (3), 183−191.

(5) Park, S.; Ruoff, R. S. Chemical Methods for the Production of Graphenes. *Nat. Nanotechnol.* **2009**, *4* (4), 217−224.

(6) Wu, D.; Zhang, F.; Liang, H.; Feng, X. Nanocomposites and Macroscopic Materials: Assembly of Chemically Modified Graphene Sheets. *Chem. Soc. Rev.* **2012**, *41* (18), 6160.

(7) Parvez, K.; Yang, S.; Hernandez, Y.; Winter, A.; Turchanin, A.; Feng, X.; Müllen, K. Nitrogen-Doped Graphene and Its Iron-Based Composite As Efficient Electrocatalysts for Oxygen Reduction Reaction. *ACS Nano* **2012**, *6* (11), 9541−9550.

(8) Hosseinzadeh, S.; Jamilpanah, L.; Shoa e Gharehbagh, J.; Behboudnia, M.; Tiwari, A.; Mohseni, S. M. Effect of YIG Nanoparticle Size and Clustering in Proximity-Induced Magnetism in Graphene/YIG Composite Probed with Magnetoimpedance Sensors: Towards Improved Functionality, Sensitivity and Proximity Detection. *Composites, Part B* **2019**, *173*, 106992.

(9) Huang, X.; Tan, C.; Yin, Z.; Zhang, H. 25th Anniversary Article: Hybrid Nanostructures Based on Two-Dimensional Nanomaterials. *Adv. Mater.* **2014**, *26* (14), 2185−2204.

(10) Pumera, M. Graphene in Biosensing. *Mater. Today* **2011**, *14* (7−8), 308−315.

(11) Liu, Z.; Robinson, J. T.; Sun, X.; Dai, H. PEGylated Nanographene Oxide for Delivery of Water-Insoluble Cancer Drugs. *J. Am. Chem. Soc.* **2008**, *130* (33), 10876−10877.

(12) Wang, C.; Han, X.; Xu, P.; Zhang, X.; Du, Y.; Hu, S.; Wang, J.; Wang, X. The Electromagnetic Property of Chemically Reduced Graphene Oxide and Its Application as Microwave Absorbing Material. *Appl. Phys. Lett.* **2011**, *98* (7), 072906.

(13) Chen, C.; Xi, J.; Zhou, E.; Peng, L.; Chen, Z.; Gao, C. Porous Graphene Microflowers for High-Performance Microwave Absorption. *Nano-Micro Lett.* **2018**, *10* (2), 26.

(14) Schedin, F.; Geim, A. K.; Morozov, S. V.; Hill, E. W.; Blake, P.; Katsnelson, M. I.; Novoselov, K. S. Detection of Individual Gas Molecules Adsorbed on Graphene. *Nat. Mater.* **2007**, *6* (9), 652−655.

(15) Sheykhifard, Z.; Mohseni, S. M.; Tork, B.; Hajiali, M. R.; Jamilpanah, L.; Rahmati, B.; Haddadi, F.; Hamdi, M.; Mohseni, S. M.; Mohammadbeigi, M.; Ghaderi, A.; Erfanifam, S.; Dashtdar, M.; Feghhi, F.; Ansari, N.; Pakdel, S.; Pourfath, M.; Hosseinzadegan, A.; Bahreini, M.; Tavassoli, S. H.; Ranjbar, M.; Banuazizi, S. A. H.; Chung, S.; Akerman, J.; Nikkam, N.; Sohrabi, A.; Roozmeh, S. E. Magnetic Graphene/Ni-Nano-Crystal Hybrid for Small Field Magnetoresistive Effect Synthesized via Electrochemical Exfoliation/Deposition Technique. *J. Mater. Sci.: Mater. Electron.* **2018**, *29* (5), 4171−4178.

(16) Wei, W.; Wang, G.; Yang, S.; Feng, X.; Müllen, K. Efficient Coupling of Nanoparticles to Electrochemically Exfoliated Graphene. *J. Am. Chem. Soc.* **2015**, *137* (16), 5576−5581.

(17) Yin, P. T.; Shah, S.; Chhowalla, M.; Lee, K.-B. Design, Synthesis, and Characterization of Graphene-Nanoparticle Hybrid Materials for Bioapplications. *Chem. Rev.* **2015**, *115* (7), 2483−2531.

(18) Lee, J.; Takemura, K.; Kato, C. N.; Suzuki, T.; Park, E. Y. Binary Nanoparticle Graphene Hybrid Structure-Based Highly Sensitive Biosensing Platform for Norovirus-Like Particle Detection. *ACS Appl. Mater. Interfaces* **2017**, *9* (32), 27298−27304.

(19) Yang, J.; Liu, P.; Wei, X.; Luo, W.; Yang, J.; Jiang, H.; Wei, D.; Shi, R.; Shi, H. Surface Engineering of Graphene Composite

DOI: 10.1021/acsaelm.9b00485
ACS Appl. Electron. Mater. XXXX, XXX, XXX−XXX

Transparent Electrodes for High-Performance Flexible Triboelectric Nanogenerators and Self-Powered Sensors. *ACS Appl. Mater. Interfaces* **2017**, *9* (41), 36017−36025.
(20) Phan, M.-H.; Peng, H.-X. Giant Magnetoimpedance Materials: Fundamentals and Applications. *Prog. Mater. Sci.* **2008**, *53* (2), 323−420.
(21) Wang, T.; Zhou, Y.; Lei, C.; Luo, J.; Xie, S.; Pu, H. Magnetic Impedance Biosensor: A Review. *Biosens. Bioelectron.* **2017**, *90*, 418−435.
(22) Buznikov, N. A.; Safronov, A. P.; Orue, I.; Golubeva, E. V.; Lepalovskij, V. N.; Svalov, A. V.; Chlenova, A. A.; Kurlyandskaya, G. V. Modelling of Magnetoimpedance Response of Thin Film Sensitive Element in the Presence of Ferrogel: Next Step toward Development of Biosensor for in-Tissue Embedded Magnetic Nanoparticles Detection. *Biosens. Bioelectron.* **2018**, *117* (May), 366−372.
(23) Panina, L. V.; Mohri, K. Magneto-impedance Effect in Amorphous Wires. *Appl. Phys. Lett.* **1994**, *65* (9), 1189−1191.
(24) Knobel, M.; Vázquez, M.; Kraus, L. Giant Magnetoimpedance. *In Handbook of Magnetic Materials* **2003**, *15*, 497−563.
(25) Moradi, M.; Hajiali, M.; Khezri, M.; Roozmeh, S. E.; Mohseni, S. M. Structural Characterization and Magnetoimpedance Effect of Current Annealed Co-Based Amorphous Ribbons at Different Ambient. *J. Supercond. Novel Magn.* **2015**, *28* (1), 265−269.
(26) Hajiali, M.; Mohseni, S. M.; Roozmeh, S. E.; Moradi, M. Asymmetric Magnetoimpedance Effect in CoFeSiB Amorphous Ribbons by Combination of Field and Current Annealing for Sensor Applications. *Superlattices Microstruct.* **2016**, *96*, 191−197.
(27) Jamilpanah, L.; Hajiali, M. R.; Mohseni, S. M.; Erfanifam, S.; Mohseni, S. M.; Houshiar, M.; Roozmeh, S. E. Magnetoimpedance Exchange Coupling in Different Magnetic Strength Thin Layers Electrodeposited on Co-Based Magnetic Ribbons. *J. Phys. D: Appl. Phys.* **2017**, *50* (15), 155001.
(28) Jamilpanah, L.; Azadian, S.; Shoa e Gharehbagh, J.; Haghniaz Jahromi, S.; Sheykhifard, Z.; Hosseinzadeh, S.; Erfanifam, S.; Hajiali, M. R.; Tehranchi, M. M.; Mohseni, S. M. Electrophoretic Deposition of Graphene Oxide on Magnetic Ribbon: Toward High Sensitive and Selectable Magnetoimpedance Response. *Appl. Surf. Sci.* **2018**, *447*, 423−429.
(29) Haj Ali, M. R.; Khezri, M.; Roozmeh, S. E.; Moradi, M.; Mohseni, S. M. The Effect of Mechanical Polishing on Current Annealed $Co_{67}Fe_5Si_{15}B_{13}$ Amorphous Ribbons: Magneto-impedance Response. *Eur. Phys. J.: Appl. Phys.* **2014**, *65* (1), 10601.
(30) Dadsetan, A.; Kashi, M. A.; Mohseni, S. M.; Hajiali, M. R. Effect of Sputter Deposited ZnO Thin Layers on Magnetoimpedance Response and Field Sensitivity of Co-Based Micro-Wires. 2018, arXiv:1811.00259. arXiv preprint archive. https://arxiv.org/abs/1811.00259.
(31) Laurita, N.; Chaturvedi, A.; Bauer, C.; Jayathilaka, P.; Leary, A.; Miller, C.; Phan, M.-H.; McHenry, M. E.; Srikanth, H. Enhanced Giant Magnetoimpedance Effect and Field Sensitivity in Co-Coated Soft Ferromagnetic Amorphous Ribbons. *J. Appl. Phys.* **2011**, *109* (7), 07C706.
(32) Chaturvedi, A.; Stojak, K.; Laurita, N.; Mukherjee, P.; Srikanth, H.; Phan, M.-H. Enhanced Magnetoimpedance Effect in Co-Based Amorphous Ribbons Coated with Carbon Nanotubes. *J. Appl. Phys.* **2012**, *111* (7), 07E507.
(33) Ruiz, A.; Mukherjee, D.; Devkota, J.; Hordagoda, M.; Witanachchi, S.; Mukherjee, P.; Srikanth, H.; Phan, M. H. Enhanced Giant Magneto-Impedance Effect in Soft Ferromagnetic Amorphous Ribbons with Pulsed Laser Deposition of Cobalt Ferrite. *J. Appl. Phys.* **2013**, *113* (17), 17A323.
(34) Hajiali, M. R.; Jamilpanah, L.; Gharehbagh, J. S. e; Azizmohseni, S.; Hamdi, M.; Mohseni, M.; Jafari, G. R.; Mohseni, S. M. Independence of Spin-Orbit-Torque from Exchange-Bias Probed via Training Effect in IrMn-Layer/Ferromagnetic-Ribbon Heterostructures. 2018, arXiv:1811.01352. arXiv preprint archive. https://arxiv.org/abs/1811.01352.
(35) Low, C. T. J.; Walsh, F. C.; Chakrabarti, M. H.; Hashim, M. A.; Hussain, M. A. Electrochemical Approaches to the Production of Graphene Flakes and Their Potential Applications. *Carbon* **2013**, *54*, 1−21.
(36) Hall, D. S.; Lockwood, D. J.; Bock, C.; MacDougall, B. R. Nickel Hydroxides and Related Materials: A Review of Their Structures, Synthesis and Properties. *Proc. R. Soc. London, Ser. A* **2015**, *471* (2174), 20140792−20140792.
(37) Bai, L.-Z.; Zhao, D.-L.; Xu, Y.; Zhang, J.-M.; Gao, Y.-L.; Zhao, L.-Y.; Tang, J.-T. Inductive Heating Property of Graphene Oxide-Fe3O4 Nanoparticles Hybrid in an AC Magnetic Field for Localized Hyperthermia. *Mater. Lett.* **2012**, *68*, 399−401.
(38) Peng, E.; Choo, E. S. G.; Chandrasekharan, P.; Yang, C.-T.; Ding, J.; Chuang, K.-H.; Xue, J. M. Synthesis of Manganese Ferrite/Graphene Oxide Nanocomposites for Biomedical Applications. *Small* **2012**, *8* (23), 3620−3630.
(39) Philip, M. R.; Narayanan, T. N.; Praveen Kumar, M.; Arya, S. B.; Pattanayak, D. K. Self-Protected Nickel-Graphene Hybrid Low Density 3D Scaffolds. *J. Mater. Chem. A* **2014**, *2* (45), 19488−19494.
(40) Liu, M.; Xu, Y.; Niu, F.; Gooding, J. J.; Liu, J. Carbon Quantum Dots Directly Generated from Electrochemical Oxidation of Graphite Electrodes in Alkaline Alcohols and the Applications for Specific Ferric Ion Detection and Cell Imaging. *Analyst* **2016**, *141* (9), 2657−2664.
(41) Naebe, M.; Wang, J.; Amini, A.; Khayyam, H.; Hameed, N.; Li, L. H.; Chen, Y.; Fox, B. Mechanical Property and Structure of Covalent Functionalised Graphene/Epoxy Nanocomposites. *Sci. Rep.* **2015**, *4* (1), 4375.
(42) Wang, Z.; Hu, Y.; Yang, W.; Zhou, M.; Hu, X. Facile One-Step Microwave-Assisted Route towards Ni Nanospheres/Reduced Graphene Oxide Hybrids for Non-Enzymatic Glucose Sensing. *Sensors* **2012**, *12* (4), 4860−4869.
(43) Li, B.; Ai, M.; Xu, Z. Mesoporous β-Ni(OH)2: Synthesis and Enhanced Electrochemical Performance. *Chem. Commun.* **2010**, *46* (34), 6267.
(44) Grossman, J. H.; McNeil, S. E. Nanotechnology in Cancer Medicine. *Phys. Today* **2012**, *65* (8), 38−42.
(45) Miller, M. M.; Prinz, G. A.; Cheng, S.-F.; Bounnak, S. Detection of a Micron-Sized Magnetic Sphere Using a Ring-Shaped Anisotropic Magnetoresistance-Based Sensor: A Model for a Magnetoresistance-Based Biosensor. *Appl. Phys. Lett.* **2002**, *81* (12), 2211−2213.
(46) Ferreira, H. A.; Graham, D. L.; Freitas, P. P.; Cabral, J. M. S. Biodetection Using Magnetically Labeled Biomolecules and Arrays of Spin Valve Sensors (Invited). *J. Appl. Phys.* **2003**, *93* (10), 7281−7286.
(47) Rife, J. C.; Miller, M. M.; Sheehan, P. E.; Tamanaha, C. R.; Tondra, M.; Whitman, L. J. Design and Performance of GMR Sensors for the Detection of Magnetic Microbeads in Biosensors. *Sens. Actuators, A* **2003**, *107* (3), 209−218.
(48) Kurlyandskaya, G. V.; Fernández, E.; Safronov, A. P.; Svalov, A. V.; Beketov, I.; Beitia, A. B.; García-Arribas, A.; Blyakhman, F. A. Giant Magnetoimpedance Biosensor for Ferrogel Detection: Model System to Evaluate Properties of Natural Tissue. *Appl. Phys. Lett.* **2015**, *106* (19), 193702.
(49) Kumar, A.; Mohapatra, S.; Fal-Miyar, V.; Cerdeira, A.; García, J. A.; Srikanth, H.; Gass, J.; Kurlyandskaya, G. V. Magnetoimpedance Biosensor for Fe3O4 Nanoparticle Intracellular Uptake Evaluation. *Appl. Phys. Lett.* **2007**, *91* (14), 143902.
(50) Dasari Shareena, T. P.; McShan, D.; Dasmahapatra, A. K.; Tchounwou, P. B. A Review on Graphene-Based Nanomaterials in Biomedical Applications and Risks in Environment and Health. *Nano-Micro Lett.* **2018**, *10* (3), 53.
(51) Denmark, D. J.; Bustos-Perez, X.; Swain, A.; Phan, M.-H.; Mohapatra, S.; Mohapatra, S. S. Readiness of Magnetic Nanobiosensors for Point-of-Care Commercialization. *J. Electron. Mater.* **2019**, *48* (8), 4749−4761.
(52) Hajiali, M. R.; Mohseni, S. M.; Jamilpanah, L.; Hamdi, M.; Roozmeh, S. E.; Mohseni, S. M. Spin-Orbit-Torque Driven Magneto-impedance in Pt-Layer/Magnetic-Ribbon Heterostructures. *Appl. Phys. Lett.* **2017**, *111* (19), 192405.

DOI: 10.1021/acsaelm.9b00485
ACS Appl. Electron. Mater. XXXX, XXX, XXX−XXX

(53) Jamilpanah, L.; Hajiali, M. R.; Mohseni, S. M.; Erfanifam, S.; Mohseni, S. M.; Houshiar, M.; Roozmeh, S. E. Magnetoimpedance Exchange Coupling in Different Magnetic Strength Thin Layers Electrodeposited on Co-Based Magnetic Ribbons. *J. Phys. D: Appl. Phys.* **2017**, *50* (15), 155001.
(54) Eggers, T.; Lam, D. S.; Thiabgoh, O.; Marcin, J.; Švec, P.; Huong, N. T.; Škorvánek, I.; Phan, M. H. Impact of the Transverse Magnetocrystalline Anisotropy of a Co Coating Layer on the Magnetoimpedance Response of FeNi-Rich Nanocrystalline Ribbon. *J. Alloys Compd.* **2018**, *741*, 1105−1111.
(55) Yang, Z.; Lei, C.; Sun, X.; Zhou, Y.; Liu, Y. Enhanced GMI Effect in Tortuous-Shaped Co-Based Amorphous Ribbons Coated with Graphene. *J. Mater. Sci.: Mater. Electron.* **2016**, *27* (4), 3493−3498.
(56) Le, A.-T.; Giang, C. D.; Tam, L. T.; Tuan, T. Q.; Phan, V. N.; Alonso, J.; Devkota, J.; Garaio, E.; García, J. Á.; Martín-Rodríguez, R.; Fdez-Gubieda, M. L.; Srikanth, H.; Phan, M.-H. Enhanced Magnetic Anisotropy and Heating Efficiency in Multi-Functional Manganese Ferrite/Graphene Oxide Nanostructures. *Nanotechnology* **2016**, *27* (15), 155707.
(57) Zhang, Y.; Huang, C.; Duan, Z.; Liu, Q.; Wang, J.; Shi, W. Enhanced Magnetoimpedance Effect of Fe 75.5 Cu 1 Nb 3 Si 13.5 B 7 Ribbon Covered by in-Situ Growth Vertical Graphene Sheets. *Mater. Lett.* **2018**, *222*, 131−134.
(58) Gromov, A.; Korenivski, V.; Haviland, D.; van Dover, R. B. Analysis of Current Distribution in Magnetic Film Inductors. *J. Appl. Phys.* **1999**, *85* (8), 5202−5204.
(59) Panina, L. V.; Mohri, K.; Uchiyama, T.; Noda, M.; Bushida, K. Giant Magneto-Impedance in Co-Rich Amorphous Wires and Films. *IEEE Trans. Magn.* **1995**, *31* (2), 1249−1260.

DOI: 10.1021/acsaelm.9b00485
ACS Appl. Electron. Mater. XXXX, XXX, XXX−XXX